Optimal Maneuvering of Seismic Sensors for Localization of Subsurface Targets

Mubashir Alam, *Student Member*, Volkan Cevher, *Member*, James H. McClellan, *Fellow*,
Gregg D. Larson, Waymond R. Scott Jr., *Senior Member*

***Abstract*— We consider the problem of detecting and locating subsurface objects by using a maneuvering array that receives scattered seismic surface waves. We demonstrate an adaptive system that moves an array of receivers according to an optimal positioning algorithm based on the theory of optimal experiments. The goal is to minimize the number of distinct measurements (array movements) needed to localize objects such as buried landmines. The adaptive localization algorithm has been tested using data collected in a laboratory facility. The performance of the algorithm is exhibited for cases with one or two targets, and in the presence of common types of clutter such as rocks in the soil. Results are also shown for a case where the propagation properties of the medium vary spatially. In these tests, the landmines were located using three or four array movements. It is envisioned that future systems could incorporate this new method into a portable mobile mine-location system.**

I. Introduction

Buried landmines and similar subsurface structures pose a huge threat to resettling civilians. It takes significant time and resources to clear out regions contaminated by mines, so it is important to develop efficient detection and localization systems to find the mines. Existing systems are usually based on Ground Penetrating Radar (GPR) and Electromagnetic Induction (EMI) sensing, but recent efforts [1]–[6] have employed seismic waves to detect subsurface targets.

To detect a landmine, a seismic wave is excited by a source at a known position and travels through the soil to interact with underground objects. The resulting propagating waves in an elastic medium are of two main types: surface waves and body waves. This paper concentrates on reflected surface waves (Rayleigh waves) for locating mines, because the Rayleigh waves carry most of the returned energy. The seismic waves are sensitive to differences in the mechanical properties of the soil, mines and clutter, while GPR and EMI sensors respond to the electrical properties. The mechanical properties and structure of a landmine are quite different from typical forms of clutter. The dominant feature of the response of a buried mine is a soil-loaded resonance of the mine case and trigger mechanism [2], [7]. This resonance causes an enhanced and sustained motion of the soil above the mine thus enhancing the waves scattered from the mine. Hence, it is possible to use seismic imaging to discriminate landmines from common types of clutter such as rocks, wood, etc.

The authors are with the School of ECE, Georgia Institute of Technology, Atlanta GA 30332-0250. This work supported by an ARO-MURI grant (DAAD19-02-1-0252): "Multi-Modal Inverse Scattering for Detection and Classification of General Concealed Targets."

Previous work on the seismic detection of landmines can be divided into two categories: methods that measure the seismic wave field directly above a mine and those that only measure a portion of the wave field at a stand-off distance [4], [5]. The first technique has been shown to be relatively resistant to clutter due to the strong resonant response directly above the mine; however, this method is quite time consuming due to the large number of measurements needed to ensure that some of the measurement points are above the mine [3], [6], [7]. Efforts to speed up these techniques using large arrays of sensors are ongoing [8], [9]. The second technique is more sensitive to clutter because the resonant response is much more difficult to isolate in the scattered waves; however, it is potentially much faster because fewer measurements are needed. Although the stand-off recordings might be made by a moving sensor, in previous work the movement of the sensor was not controlled adaptively in response to processing.

In this paper, we develop a technique that combines the strengths of the above techniques. We show how a small array that makes its first recording at some distance from a target can be moved to new recording positions that will increase the ability of the system to find the target's location. The array movements are done in an optimal fashion to maximize the "information gained" about the target at each iteration. In our case, we use a small 3×3 array, so any one image has low resolution. However, as the array maneuvers, we can accumulate the measurements, and the cumulative imaging operation improves the resolution around the target location by increasing the effective aperture. After the target is located, a *confirmation* step would be performed to decide whether the target is a landmine by using an imaging technique that enhances the resonance, e.g., [10].

One applicable theory for optimal sensor placement is the "theory of optimal experiments" [11], which predicts the results of experiments based on information-theoretic concepts. These methods use some form of the Fisher information matrix, from which the Cramer-Rao bound is obtained. Various measures of Fisher information are possible, giving different design criteria, but this paper concentrates on D-optimal design which maximizes the determinant of the Fisher information matrix. An example of using the method of optimal experiments for sensor placement can be found in [12], [13], which deals with the movement of sensors used in direction-of-arrival (DOA) estimation to localize a source. The D-optimal criterion is equivalent to minimizing the trace of the Cramer-Rao lower bound (CRLB), so the result is an optimal observer (sensor) path that localizes a moving source. In [14], a single moving

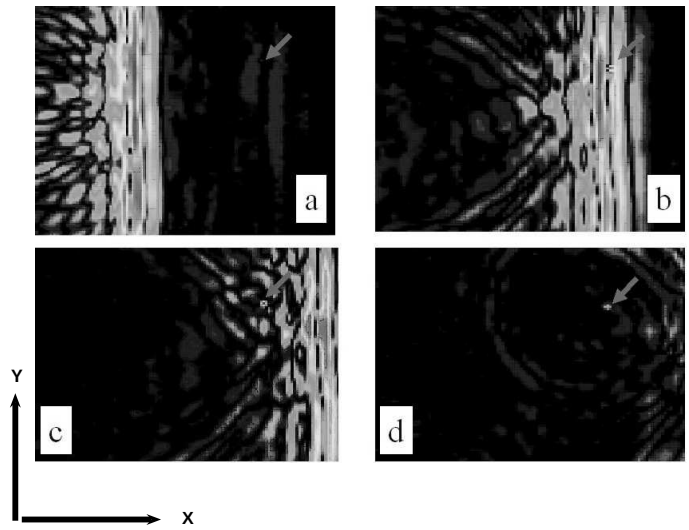

Fig. 1. Surface displacement plots showing wave propagation. TS-50 landmine location denoted by an arrow (40 dB scale). (a) Rayleigh wave approaching the mine, (b) wave reaches the top of the mine, (c) main pulse passes the mine, (d) scattered wave with mine still resonating.

sensor is used to localize a vapor emitting source by estimating the location of the source and minimizing its CR bound at each step. A recent example of D-optimal experiment design involves moving an EMI sensor to locate buried targets [15], and, in [16], D-optimal design is used for optimal sensor placement to solve an inverse problem.

The paper is organized as follows. Section II describes the steps in the algorithm including the performance bounds on target location estimates from which the D-optimal maneuver algorithm is derived. Section III contains the results of applying the new algorithm to data collected in a laboratory setting for scenarios with single targets, multiple targets, and clutter.

II. Target Location and Sensor Maneuver Method

The proposed optimal maneuvering algorithm is an iteration that involves three main steps: The first is identification of the seismic wave components and separation of the reflected wave from the incident wave; the second is near-field imaging with a propagation model to estimate the target location; and the third is the optimal maneuver calculation to reposition the receiving array for the next iteration. During the first step, different seismic wave components have to be identified and separated, because the imaging in the second step must be done with only reflected waves. The system uses an active source that is also in the vicinity of the receivers, so the array will also record a very strong forward wave. For example, the raw collected data at four time instants from a TS-50 (anti-personnel) landmine buried at a depth of 1 cm is shown in Fig. 1. This figure shows the strong forward seismic wave approaching the mine during the first two frames, and reflecting from the mine in the third. In the last frame the weak reflection from the mine can be seen clearly.

If the target is far from the receivers, we can remove the forward wave with a time gate, but when the target is nearby, the two waves tend to overlap in time. A frequency-domain algorithm based on Prony's method is used to first identify different wave components and then separate them [17], [18]. This analysis technique requires a linear array of sensors to collect the space-time data (10 or 15 sensors suffices). At present, we use a 3×10 array and perform the wave separation on each ten-element linear subarray. Then a 3×3 subarray is retained for the imaging and optimal maneuvering steps.

After the waves have been separated, the next step is to image the targets to find their locations. The applicable data model for the reflected waves is the classical model used in passive array processing. The imaging algorithm works in the frequency domain, even though the received sensor data is not narrowband. The nature of the seismic waves suggests that frequency domain processing is more suitable for two reasons. First, soil is usually a highly dispersive medium, where propagation velocity varies with frequency. Second, targets at various depths can be imaged by varying the frequency content of the probing pulse. Thus, we formulate a propagation model and steering vectors that can be used when velocity varies with frequency.

One goal is to design the system so that the array can be placed on a mobile platform, which can maneuver as it senses the environment. Therefore, the size of the array has to be small, which means a small aperture. This small aperture will result in low resolution or higher uncertainty about the location estimate of the target. One way to increase resolution is to increase the effective aperture by moving the array and forming a synthetic aperture. Hence, the algorithm that determines the next optimal position for the array must also accumulate its measurements from several positions.

The system maneuvers based on its present estimate of the target location. The 2-D sensor array estimates the target location with an imaging algorithm. Then, the variance of the location estimate is calculated by using the Fisher information matrix (FIM), assuming the location estimate is the true target location. Based on the expected value of the FIM, the next optimal array position is calculated by using the theory of optimal experiments [11], [15], specifically, D-optimal design which maximizes the determinant of the FIM. The two steps involved in the maneuver strategy for a mobile array of sensors are shown in Figs. 2(a) and 2(b).

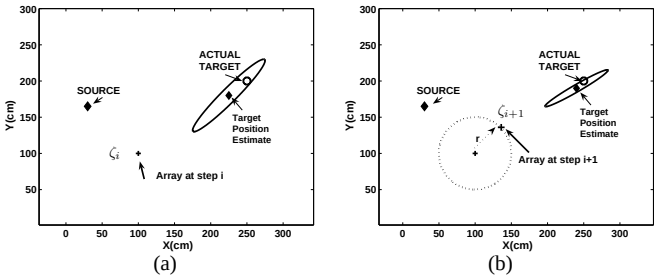

Fig. 2. Algorithm steps illustrated: (a) The source generates a probing pulse. Waves scattered from the target are collected by the receiving array. At step i, the target location $\mathbf{z}_i$ is estimated when the array center is at $\boldsymbol{\zeta}_i$ (b) Estimate the next array position $\boldsymbol{\zeta}_{i+1}$ by using $\mathbf{z}_i$ and the constrained cumulative Fisher Information Matrix measure along a circle.

A. Spectrum Analysis Technique for Wave Separation

The wave separation is based on a parametric modeling technique previously developed for borehole sonic logging applications [17]. The collected data $s(x,t)$ from a linear array is a function of space and time, and has a 2-D Fourier representation $\hat{S}(k,\omega)$

$$s(x,t) = \frac{1}{4\pi^2}\int_{-\infty}^{\infty}\int_{-\infty}^{\infty}\hat{S}(k,\omega)e^{j(kx-\omega t)}dk\,d\omega, \qquad (1)$$

where x is the spatial position, k the spatial wave number, and ω is temporal frequency. By taking a Fourier transform of the space-time data across t only, we obtain

$$S(x,\omega) = \frac{1}{2\pi}\int_{-\infty}^{\infty}\hat{S}(k,\omega)e^{j(kx)}dk. \qquad (2)$$

At each temporal frequency ω, exponential modeling can be done across the spatial dimension to approximate the integral in (2) with a sum (of propagating waves)

$$S(x,\omega) \approx \sum_{p=1}^{P} a_p(\omega)e^{j\kappa_p(\omega)x}, \qquad (3)$$

where P is the model order. The parameters $a_p(\omega)$ and $\kappa_p(\omega)$ are calculated with a pole-zero modeling technique based on the Iterative Quadratic Maximum Likelihood (IQML) algorithm, which is equivalent to the well-known Steiglitz-McBride extension of Prony's method [19]–[22].

The poles from IQML determine the exponents $\kappa_p(\omega) = k_p(\omega) + j\alpha_p(\omega)$ whose real part is the wave number $k_p(\omega)$ and whose imaginary part is the attenuation $\alpha_p(\omega)$. Wave number can be converted to phase velocity via $v_p(\omega) = \omega/k_p(\omega)$, and then we can plot the magnitude of a_p versus frequency and velocity. This type of plot is a 2-D velocity-frequency spectrum, e.g., Fig. 3(b), from which it is easy to obtain the dispersion curves for the various modes that make up the signal. The complex amplitudes a_p determine the strength of different wave components. Furthermore, the individual modes of $s(x,t)$ can be identified and grouped according to velocity $v_p(\omega)$ and frequency. Once we have sorted out a single mode in the velocity-frequency domain, it is possible to reconstruct the waveform for that mode in the space-time domain by using the model

$$s(x,t) = \sum_i a(\omega_i)e^{(\alpha(\omega_i)x + j(\omega_i t + k(\omega_i)x))}. \qquad (4)$$

where the sum would include only those parameters $a(\omega_i)$, $\alpha(\omega_i)$ and $k(\omega_i)$ corresponding to the mode of interest.

This processing has been applied to data collected in the laboratory and in the field, and used to extract waves reflected from buried targets [22]. For example, consider the setup shown in Fig. 3(a), where a linear array lies between the source and the target. The target in this case is a VS-1.6 anti-tank landmine buried at a depth of 8 cm. The array consists of ten sensors (ground contacting accelerometers) with an inter-sensor spacing of 3.4 cm. The resulting velocity-frequency spectrum is shown in Fig. 3(b). The analysis easily separates

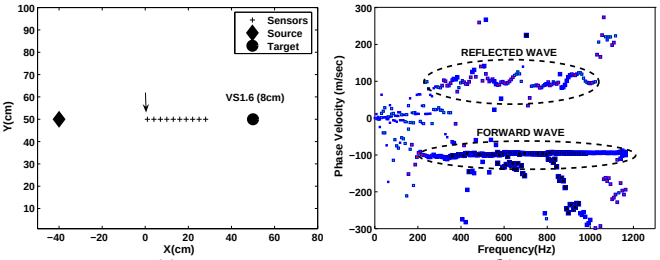

(a) (b)

Fig. 3. (a) Array setup with linear array between the source and target. The first sensor position is indicated by the arrow. (b) Spectrum analysis: reflected waves have positive velocity; forward waves, negative velocity.

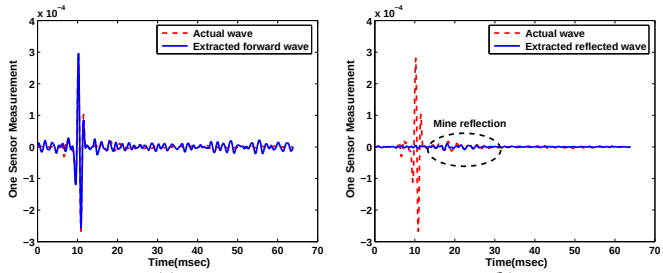

(a) (b)

Fig. 4. Reconstruction (4) using the subsets selected in Fig. 3(b). Extracted wave and original at one sensor only: (a) Forward wave, (b) Reflected wave.

the forward and reflected waves on the basis of positive and negative velocities, or equivalently, wave numbers. Once these waves are identified in Fig. 3(b), their individual parameters can be extracted, followed by reconstruction in the space-time domain using (4). The extracted forward and reverse waves at the first sensor are shown in Fig. 4, demonstrating that this method is able to separate and reconstruct these waves.

B. Target Location Estimates and Performance Bounds

Once we have extracted the reflected wave(s) we can address the problem of finding the target location(s) as a near-field array processing problem.

1) Data Model for active sensing: Consider a single seismic source illuminating K targets, and an array of P seismic receivers, where the source, targets and receivers are coplanar. Since we model the soil as a dispersive medium with frequency dependent velocity, we prefer to do the processing in the frequency domain.

The received seismic data at frequency ω can be written as

$$\mathbf{y}(\omega) = \mathbf{G}(\omega)\mathbf{D}(\omega)\mathbf{g}_1(\omega) + \mathbf{n}(\omega), \qquad (5)$$

where $\mathbf{g}_1(\omega)$ is a $K\times 1$ vector that models the propagation from the single seismic source to the targets, $\mathbf{D}(\omega)$ is a $K\times K$ diagonal matrix whose elements are the scattering coefficients from the K targets, $\mathbf{G}(\omega)$ is a $P\times K$ matrix that represents the propagation from the targets back to the receiver array, and $\mathbf{n}(\omega)$ is additive noise [23]–[26]. The elements of the propagation matrices are given by the 2-D Green's function. Since only the reflected signals are of interest, the active system in (5) can be simplified to the following equivalent passive system

$$\mathbf{y}(\omega) = \mathbf{G}(\omega)\mathbf{s}(\omega) + \mathbf{n}(\omega), \qquad (6)$$

where $\mathbf{D}(\omega)\mathbf{g}_1(\omega)$ has been replaced by a $K\times 1$ signal vector $\mathbf{s}(\omega)$ that represents the reflected signals from targets. Equation (6) has the same mathematical form as the narrow-band data model [27] used in conventional array signal processing and this similarity will be exploited while calculating the maximum likelihood location estimate.

In the seismic problem, the elements of the propagation matrix $\mathbf{G}(\omega)$ are given by the illuminating Green's vector (steering vector) [23]–[25], [28],

$$\mathbf{g}(\mathbf{z},\mathbf{x},\omega) = [\tilde{g}(\mathbf{z},\mathbf{x}_1,\omega),\ldots,\tilde{g}(\mathbf{z},\mathbf{x}_P,\omega)]^T, \qquad (7)$$

where $\mathbf{z}$ is the target location, $\mathbf{x}_i$ the i^{th} sensor position in the 2-D plane, and $\tilde{g}$ the 2-D Green's function, whose analytical form is

$$\tilde{g}(r,r',\omega) = \frac{i}{4}H_0^{(1)}\left(\frac{\omega}{v(\omega)}|r-r'|\right), \qquad (8)$$

where $H_0^{(1)}$ is the zero-order Hankel function of the first kind, and $v(\omega)$ is the frequency-dependent Rayleigh wave velocity, which is an accurate model for a vertically stratified media, but an approximate model in the presence of lateral inhomogeneities. Spectrum analysis of the surface waves [22] (Section II-A) is used to determine $v(\omega)$.

To minimize confusion when we refer to existing array processing literature results, we change the notation for the propagation matrix from $\mathbf{G}$ to $\mathbf{A}$ (called the steering matrix), and the final form of the data model becomes [27]:

$$\mathbf{y}(\omega) = \mathbf{A}(\boldsymbol{\zeta},\mathbf{z},\omega)\mathbf{s}(\omega) + \mathbf{n}(\omega), \qquad (9)$$

where $\mathbf{y}(\omega)$ is the array output vector, $\mathbf{n}(\omega)$ is complex additive noise, and $\mathbf{s}(\omega)$ is the signal vector. The steering matrix $\mathbf{A}(\boldsymbol{\zeta},\mathbf{z},\omega)$ has elements given by the Green's function (7), which depends on the array center position $\boldsymbol{\zeta}$ and the (unknown) target location $\mathbf{z}$. Our objective is to determine the target location(s) $\mathbf{z}$ given the received array data $\mathbf{y}(\omega)$.

2) Target Location Estimation: Let the data vector $\mathbf{Y} = \left[\ \mathbf{y}^T(\omega_1)\ ,\ \ldots\ ,\ \mathbf{y}^T(\omega_N)\ \right]^T$, $\mathbf{Y}\in\mathcal{C}^{PN\times 1}$, be formed by aggregating the Fourier transform of $\mathbf{y}$ at N frequencies, ω_i. Under the assumption of independent, identically distributed (*i.i.d.*) Gaussian noise, the likelihood function (a probability density) for the current received data [29] is:

$$p(\mathbf{Y}) = \prod_{l=1}^{N}\frac{1}{\pi^P\sigma_n^{2P}}\exp\left\{-\frac{1}{\sigma_n^2}\|\mathbf{y}(\omega_l)-\mathbf{A}(\omega_l)\mathbf{s}(\omega_l)\|^2\right\} \qquad (10)$$

From (10), we obtain the negative log-likelihood function

$$L^- = NP\log(\pi\sigma_n^2) + \frac{1}{\sigma_n^2}\sum_{l=1}^{N}\|\mathbf{y}(\omega_l)-\mathbf{A}(\omega_l)\mathbf{s}(\omega_l)\|^2. \qquad (11)$$

and the Maximum-Likelihood (ML) estimate is determined by minimizing L^-. In (11), both the target signal and the noise variance are unknown, but the gradient of L^- is separable so that we can first solve for the noise variance from the derivative of L^- with respect to σ_n^2

$$\hat{\sigma}_n^2 = \frac{1}{NP}\sum_{l=1}^{N}\|\mathbf{y}(\omega_l)-\mathbf{A}(\omega_l)\mathbf{s}(\omega_l)\|^2. \qquad (12)$$

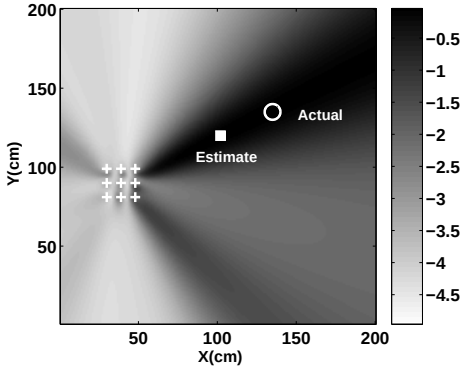

Fig. 5. Target location estimate done using the ML cost function (14); inverse of $J(\mathbf{z})$ is plotted (dB scale).

Using (12) we can then solve for the signal from the derivative of L^- with respect to $\hat{s}(\omega_l)$

$$\hat{s}(\omega_l) = \left(\mathbf{A}^H(\omega_l)\mathbf{A}(\omega_l)\right)^{-1}\mathbf{A}^H(\omega_l)\mathbf{y}(\omega_l), \qquad (13)$$

where $\mathbf{A}^H$ is complex conjugate transpose of $\mathbf{A}$. Substituting (12) and (13) into (11), we can rewrite the ML cost function that must be minimized as a function of $\mathbf{z}$

$$\begin{aligned} J(\mathbf{z}) &= \sum_{l=1}^{N}\left\|\left(I-\mathbf{A}(\omega_l)\left(\mathbf{A}^H(\omega_l)\mathbf{A}(\omega_l)\right)^{-1}\mathbf{A}^H(\omega_l)\right)\mathbf{y}(\omega_l)\right\|^2 \\ &= \sum_{l=1}^{N}\text{trace}\left\{P_A^{\perp}(\omega_l)R_y(\omega_l)\right\}, \end{aligned} \qquad (14)$$

where $P_A^{\perp}(\omega_l) = I-\mathbf{A}(\omega_l)\left(\mathbf{A}^H(\omega_l)\mathbf{A}(\omega_l)\right)^{-1}\mathbf{A}^H(\omega_l)$, is the projection onto the null space of $\mathbf{A}^H(\omega_l)$ and $R_y(\omega_l) = \mathbf{y}(\omega_l)\mathbf{y}^H(\omega_l)$ is the single snapshot covariance matrix estimate at ω_l. The target location estimate is then obtained by minimizing the cost function $J(\mathbf{z})$, i.e., $\mathbf{z}_{\text{est}} = \arg\min_{\mathbf{z}} J(\mathbf{z})$.

An example of estimating the target location for the TS-50 data in Fig. 1 is shown with the surface plot in Fig. 5. The surface plot (of the the inverse of $J(\mathbf{z})$) was obtained by using (14) and evaluating this cost function at each point $\mathbf{z}$ over a 2-D grid. The target location estimate is the minimum indicated with a square.

3) Cramer-Rao Lower Bound for the Estimate of $\mathbf{z}$*:* The Cramer-Rao lower bound (CRLB) is an information theoretic inequality which provides a lower bound for the variances of the unbiased estimators. If an estimator achieves the CRLB, then it is also a solution of the likelihood equation. The Cramer-Rao lower bound is the inverse of the Fisher information matrix (FIM). Assuming that the variance of the additive noise in (5) is known, the log-likelihood function (11) for a *single target* has one term that depends on $\mathbf{z}$:

$$L(\boldsymbol{\zeta},\mathbf{z}) \doteq -\frac{1}{\sigma_n^2}\sum_{l=1}^{N}\|\mathbf{y}(\omega_l)-\mathbf{a}(\boldsymbol{\zeta},\mathbf{z},\omega_l)s(\omega_l)\|^2, \qquad (15)$$

where $\mathbf{a}(\boldsymbol{\zeta},\mathbf{z},\omega)$ is the propagation (steering) vector from the array center $\boldsymbol{\zeta}$ to the location estimate $\mathbf{z}$. The $(i,j)^{\text{th}}$ element of the matrix $\mathbf{F}$ is given by the partial derivative of (15) with

respect to the i^{th} and j^{th} parameters of the vector $\mathbf{z}$ [29]:

$$\mathbf{F}_{i,j}(\mathbf{z},\boldsymbol{\zeta}) = E_y\left\{\frac{\partial^2 L(\mathbf{z},\boldsymbol{\zeta})}{\partial z_i\,\partial z_j}\right\} = -\frac{2}{\sigma_n^2}\sum_{l=1}^{N}\Re\left\{\left(\frac{\partial \mathbf{a}(\mathbf{z},\boldsymbol{\zeta},\omega_l)}{\partial z_i}\right)^H \frac{\partial \mathbf{a}(\mathbf{z},\boldsymbol{\zeta},\omega_l)}{\partial z_j}\right\},$$

where $E_y\{.\}$ denotes the expected value. The partial derivative of the steering vector is calculated with respect to the target coordinates for a fixed array center.

C. Movement of the Seismic Array via Optimal Experiments

Previously, we described how to determine the target location estimate and the corresponding FIM which represents the uncertainty about the estimate as a function of the array center position $\boldsymbol{\zeta}$. Suppose that we are at step i with a target location estimate $\mathbf{z}_i$ obtained when the array is at position $\boldsymbol{\zeta}_i$, and now we are interested in determining the next optimal array center position candidate $\boldsymbol{\zeta}_{i+1}$. Our approach is to select the new sensor position to reduce the expected uncertainty in the estimated target coordinates by minimizing the determinant of the CRLB, or, equivalently, by maximizing the determinant of the FIM as a function of the array center $\boldsymbol{\zeta}$. In the literature of optimal experiments, this technique is called D-optimal design [11] (see [15] for an application to magnetic sensors).

Let q represent the determinant of the FIM. The cumulative effect of the measurements up to step i can be written as:

$$q\left(\{\boldsymbol{\zeta}_1,\ldots,\boldsymbol{\zeta}_i\}\right) = \left|F(\boldsymbol{\zeta}_1,\ldots,\boldsymbol{\zeta}_i)\right| = \left|\sum_{j=1}^{i} F(\boldsymbol{\zeta}_j)\right|, \quad (16)$$

where $|\cdot|$ stands for determinant and $F(\boldsymbol{\zeta}_i)$ represents the FIM at step i. The logarithmic increase due to the additional measurements at step $i+1$ is given by

$$\begin{aligned}\delta_q(\boldsymbol{\zeta}_{i+1}) &= \ln q\left(\{\boldsymbol{\zeta}_1,\ldots,\boldsymbol{\zeta}_i,\boldsymbol{\zeta}_{i+1}\}\right) - \ln q\left(\{\boldsymbol{\zeta}_1,\ldots,\boldsymbol{\zeta}_i\}\right)\\ &= \ln\left|I + F(\boldsymbol{\zeta}_{i+1})B_i^{-1}\right|, \end{aligned} \quad (17)$$

where I is an identity matrix, and $B_i = \sum_{j=1}^{i} F(\boldsymbol{\zeta}_j)$. Therefore, to maximize the expected information gain, the next optimal array center should be determined by

$$\boldsymbol{\zeta}_{i+1} = \arg\max_{\boldsymbol{\zeta}}\left\{\ln\left|I + F(\boldsymbol{\zeta}_{i+1})B_j^{-1}\right|\right\}. \quad (18)$$

1) Constraints: In this optimization problem (18), there are hidden constraints that come from the configuration of the seismic measurement system. First of all, we need to make sure that the *array always receives backscattered waves*. If the array lies on the far side of the target, the forward scattered waves are weak and are mixed with the very strong forward probing pulse, so it is difficult to extract the reflected wave using the Prony analysis. One way to impose this condition is to restrict the movement of the array center to be less than a fixed step size of r. In effect, this means that we calculate the maximum of (18) on a circle of radius r, with the center of the circle at the previous optimum array center position.

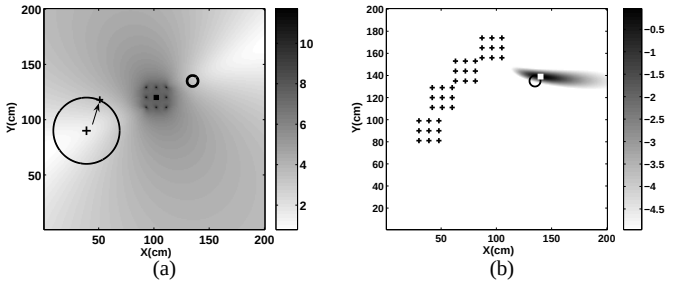

Fig. 6. (a) Circle constraint for optimum movement to the next array position. Mine location is indicated by smaller circle. The surface plot shows the determinant of the FIM (linear scale). (b) Location estimate after the three optimal moves; inverse of $\boldsymbol{J}(\mathbf{z})$ is plotted (dB scale).

Another way to constraint the array movement would be to add a penalty term as in [15]:

$$\Psi(\boldsymbol{\zeta}) = \delta_q(\boldsymbol{\zeta}_{i+1}) - \nu\sqrt{(\boldsymbol{\zeta}_{i+1}-\boldsymbol{\zeta}_i)^T\,\Sigma^{-1}(\boldsymbol{\zeta}_{i+1}-\boldsymbol{\zeta}_i)}, \quad (19)$$

where $\nu \geq 0$ is the penalty factor that must be chosen relative to the size of $\delta_q(\boldsymbol{\zeta}_{i+1})$, and Σ is a diagonal matrix, whose diagonal elements are chosen to ensure smooth movement of the array from the previous position. However, this approach constrains the step size indirectly, and does not guarantee that the array will stay between the source and the target.

An example of the circle constraint is shown in Fig. 6(a), where a circle of radius of 25 cm is used. Based on the initial target location estimate of the TS-50 landmine in Fig. 5, the unconstrained optimal array position would be determined by using (18) evaluated at each grid point where the new array center could be located. The circle constraint restricts this evaluation to the small subset of points on the circle in Fig. 6(a), so it is also much more efficient than the unconstrained approach or the penalty function method.

Once the next optimum array position is determined and the array is moved to the new position, a new batch of data is collected. This new data is appended to the existing data, and the new target location estimate, as well as the next optimum array movement, are determined by using the cumulative data. Further steps are shown in Fig. 6(b). With each successive step the target location estimate is improved in the sense that there is a decrease in the uncertainty ellipse of the estimate. Intuitively, the explanation is that the cumulative estimation is effectively increasing the aperture.

III. Processing of Experimental Data

Several tests were conducted with anti-personnel and anti-tank landmines with and without buried clutter objects in an experimental model [2] to evaluate the optimal maneuvering algorithms. The experiments included a TS-50 anti-personnel (AP) landmine, a VS-2.2 anti-tank (AT) landmine, a VS-1.6 AT landmine, and several rocks that were similar in size to the landmines. The TS-50 is a plastic landmine, 9 cm in diameter and 4.6 cm in height; the VS-2.2 is a non-metallic landmine (24.2 cm diameter, 11.8 cm tall); and the VS-1.6 is a slightly smaller non-metallic landmine (23.3 cm diameter, 9.2 cm tall). The experimental model with the sensor array and seismic source is shown in Fig. 7. Damp, compacted

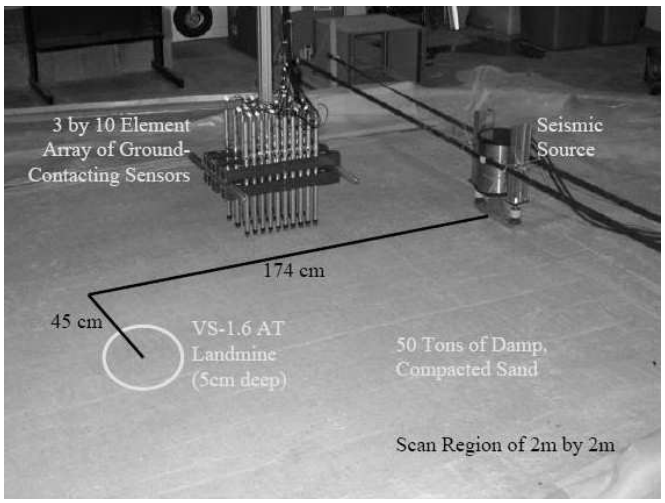

Fig. 7. Experimental setup showing the sensor array of 3×10 elements, the seismic source, and a buried target. Although the source is on the right in this photo, all figures that show processing have the source on the left.

sand has been used as a soil surrogate in the experimental model as its properties closely resemble those of typical soils [4], [5], [30]–[33], and it can easily be reconditioned for consistency amongst multiple measurements. To prepare the model for an experiment after burying landmines and clutter, the sand is wetted and packed using a hand tamper to recondition the soil as a homogeneous medium. Targets and clutter can be buried in a 2 m by 2 m scannable region in the center of the model. The seismic source is a ground-coupled electrodynamic transducer located at a fixed position approximately 40 cm from the edge of the scan region. It generates seismic waves with a 4.096 s chirp swept from 100 Hz to 2 kHz. Surface motions were measured using a 3×10 array of ground-contacting accelerometer sensors [34] with inter-element spacings of 10.2 cm and 3.4 cm. The sensor array was moved through the scan region using a computer-controlled, three-axis positioning system. Post-processing of the acquired data included convolution to shape the received pulse into a 450 Hz center-frequency differentiated Gaussian pulse prior to the processing. For typical measurements, the ambient noise is approximately 45 dB below the level of the interrogation (incident) signal, while the signal clutter level in clean sand is approximately 30 dB below the interrogation signal. The signals scattered from the mines are much weaker than the interrogation signal and are often below the level of the clutter signals.

For these experiments, a *probe phase* and a *search phase* were used. In the *probe phase*, measurements were made at two or three predetermined positions in front of the seismic source to interrogate the entire scan region for targets via the ML imaging algorithm (14) (using only one probe position was unreliable). The probe phase provides an initial low-resolution location estimate for the *search phase* which then performs the optimal maneuvers to better locate the targets. The new array positions are calculated from the FIM, and the target location is refined according to (14) and (18).

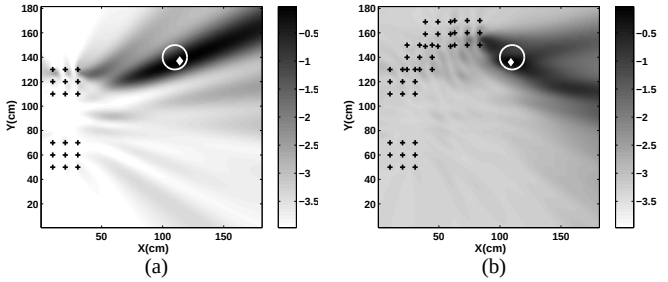

Fig. 8. Experiment S-1. Single target case: (a) After the *probe phase* (two fixed positions). (b) After three optimal moves, the resolution of the estimate around the true target location is significantly increased, and the uncertainty reduced. ML surfaces, the inverse of $\boldsymbol{J}(\mathbf{z})$, are plotted on a dB scale.

A. Single Target Case (Experiment S-1)

The first experiment involved a single VS-1.6 AT landmine buried 5 cm deep in the experimental model, as shown in Fig. 7. Figure 8(a) shows the two probe-phase measurement positions (indicated by the 3×3 array of sensor positions), the actual landmine burial location (indicated by the circle), and the initial target location estimate (indicated by the diamond) made via the ML imaging algorithm during the *probe phase*. For every 3×10 array measurement position, the data collected across each 10-element line of the array was processed by the Prony-based velocity spectrum analysis in order to separate the direct and scattered waves. The reflected waves were resynthesized at three out of the ten sensors in each line and retained to form a 3×3 array for imaging.

During the *search phase*, the optimal array movement was constrained by the circle constraint, using a 25 cm radius to control the step size. The initial and final location estimates, shown in Fig. 8(a) and (b), show the improvement in the target estimate. With the circle constraint, we observe that the array not only moves toward the target but also increases the effective array aperture, thereby reducing the size of the uncertainty ellipse around the target location estimate. The final target location estimate was directly on top of the landmine burial position. The five array measurements made in this case consist of 150 individual sensor measurements. This is a substantial reduction in the amount of data required to locate buried targets as approximately 3600 individual sensor measurements (or 120 array measurements) would be necessary to scan the entire $4\,\mathrm{m}^2$ region.

B. Single Target in Clutter (rocks)

To test the behavior of the algorithm in clutter, rocks are introduced in addition to landmines. The rocks scatter seismic waves, like land mines, so discriminating the rocks from landmines with the method of optimal maneuvers depends upon the relative strengths of their scattered waves. However, a rock that is approximately the same size and buried at the same depth as a landmine will generally scatter less than the landmine due to the resonance of the landmine. Two experiments are presented that demonstrate that the algorithm is not confused by rocks that scatter less than the landmine.

1) Experiment C-1: The first experiment is with a small TS-50 AP mine buried at a depth of 1 cm surrounded by four rocks

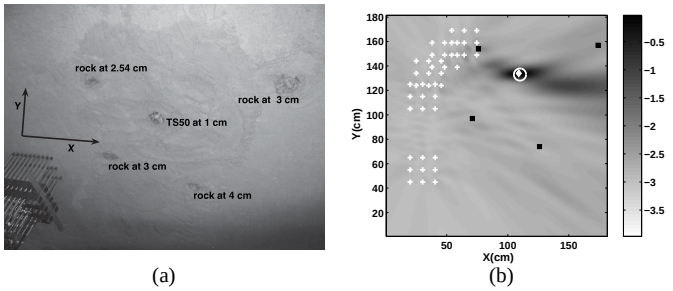

(a) (b)

Fig. 9. Experiment C-1: TS-50 surrounded by four rocks. (a) Experimental setup showing rocks and the mine. (b) Final location estimate after three optimal moves; rock positions denoted by squares.

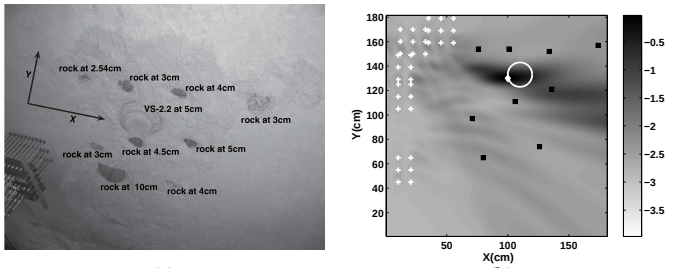

(a) (b)

Fig. 10. Experiment C-2: VS-2.2 surrounded by nine rocks. (a) Experimental setup showing rocks and the mine. (b) Final location estimate after three optimal moves; rock positions denoted by squares.

which are nearly the same size as the mine but buried deeper. The locations and burial depths of the rocks and the mine are shown in Fig. 9(a). The location estimate using optimal maneuvers is shown in Fig. 9(b), and the array is able to pick out the target in the presence of these rocks, primarily because it is close to the surface.

2) Experiment C-2: In the second experiment, Fig. 10(a), a VS-2.2 AT mine is surrounded by nine rocks, one of which is nearly as big as the VS-2.2 but buried deeper. The three optimal moves to locate the mine are shown in Fig. 10(b). Since the VS-2.2 is large and the rocks buried at shallower depths are smaller, its signature is stronger than any of the rocks. Thus the algorithm picks out the VS-2.2 from the rocks rather easily, although the final location estimate is at the front edge of the mine.

C. Multi-target case: Experiment M-1

In the first multi-target experiment, we assume that the number of targets is known. Two VS-1.6 anti-tank (AT) mines are buried at a depth of 5 cm. During the probe phase, three fixed array positions with respect to the source are used to find the starting locations for the search phase. The three fixed array positions are shown only as their centers (+ signs), but the shape and size of the array is the same 3×3 array used before. The ML estimates of the two target locations are shown in Fig. 11. Since two initial ML estimates have been obtained, the method for maneuvering the array optimally with the FIM must be modified. The FIM is now of size 4×4, so we partition the matrix into four 2×2 submatrices related to the individual targets and their cross terms.

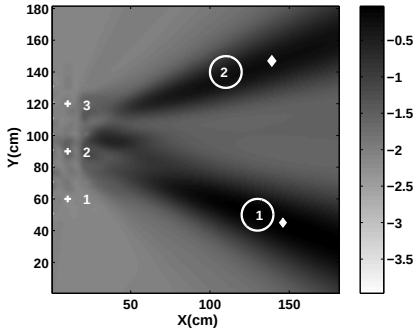

Fig. 11. Experiment M-1: Initial estimates from the *probe phase* for the two targets case. Three fixed array positions centered at 1, 2 and 3. The true locations of two targets (circles) and their initial estimates (diamonds) are also shown. ML surfaces, the inverse of $\boldsymbol{J(z)}$, are plotted on a dB scale.

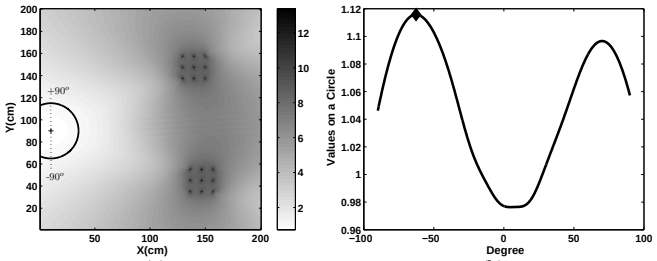

(a) (b)

Fig. 12. Experiment M-1 (two targets): Next optimal array position (linear scale). (a) Surface plot obtained using (18) with a circle of 25 cm. (b) Values along the circle from $-\mathbf{90}^\circ$ to $\mathbf{90}^\circ$ by using (17).

Since we want to minimize the determinant of the FIM as in (18), there are various options available. One is to use the full 4×4 FIM matrix in (18), and the other would be to devise a partitioned approach with the two smaller 2×2 FIMs, one for each target. The second approach is inherently more complicated and might involve multi-objective optimization to satisfy both measures.

Thus we use the 4×4 approach and determine the next array position by using (18) with a circle constraint. A circle of radius 25 cm is used, and the array center at position-2 is used as the center of the first circle. The surface obtained by using the 4×4 FIM is shown in Fig. 12(a) and the values on the circle from -90° to 90° are shown in Fig. 12(b). There are two well defined peaks with one direction favored more than the other. The higher peak in this plot is picked to generate the next optimal array position.

The succeeding array positions are obtained optimally and the surface plot at the fourth step and the last step are shown in Fig. 13(a) and (b). From this figure, we can make two interesting observations: once the optimal maneuver algorithm picks one target, the algorithm continues to move toward that target. While the array moves toward target-1, the signature of target-2 becomes weaker but does not disappear. At the last step shown in Fig. 13(b), target-1 has been localized to within its radius and there is appreciable reduction in the size of its uncertainty ellipse. However, the weak signature of target-2 is still somewhat present, and with a very accurate location estimate; most likely because the ML imaging algorithm is

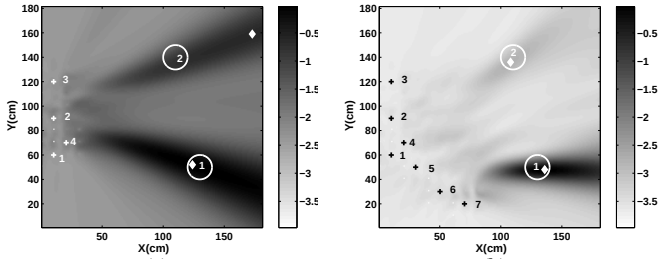

Fig. 13. Experiment M-1, two VS-1.6 landmines: (a) Optimal maneuvers up to step 4. (b) After seven steps. ML surfaces, the inverse of $\boldsymbol{J}(\mathbf{z})$, are plotted on a dB scale.

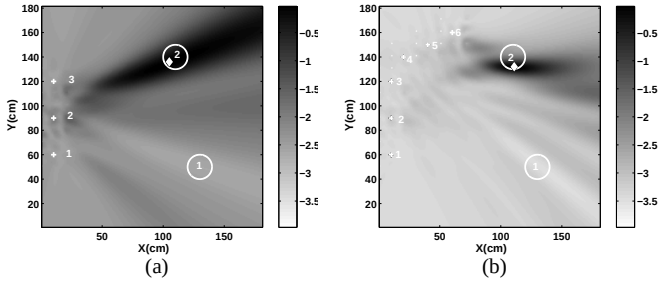

Fig. 14. Experiment M-1, two VS-1.6 landmines: estimating the second target after removing the effect of the first target from the array data. (a) Probe phase with the array at positions 1, 2 and 3. (b) Final estimate after three optimal maneuvers. ML surfaces, the inverse of $\boldsymbol{J}(\mathbf{z})$, are plotted on a dB scale.

using seven array measurements at the end.

Once we have completely localized the first target, we would return to the original starting positions and remove the effects of the already localized target from the array data. The remaining targets can then be localized. The removal technique used will be based on the CLEAN algorithm originally developed for radio astronomy [25], [35]. Suppose that there are M targets, and out of these we have estimated all the locations except for the m^{th} target. Then the "cleaned" array data at a frequency ω_l which can be used for this target is given by:

$$\mathbf{y}_m(\omega_l) = \mathbf{y}(\omega_l) - \sum_{j=1, j\neq m}^{M} \mathbf{g}(\mathbf{p}_j, \omega_l) s_j(\omega_l) \qquad (20)$$

where $\mathbf{g}$ is the steering vector whose elements are given by the known 2-D Green's function, $\mathbf{p}_j$ is the j^{th} target location estimate, and $s_j(\omega_l)$ is the signal reflected from the j^{th} target which can be estimated using (13). Once we remove the first target using (20), the FIM will be reduced to a 2×2 matrix. The probe phase for the second target uses the previous starting position as shown in Fig. 14(a), the only difference being that the effect of target-1 has now been completely removed from the array data. The next few optimal moves to locate target-2 are shown in Fig. 14(b). Now this second target has been completely localized in addition to considerable reduction in the size of its uncertainty ellipse.

D. Multi-target case: Experiment M-2

In most realistic situations, there is no *a priori* knowledge of the number of targets, and a different strategy must be developed. At each iteration, we could assume that there is only one strong target, and then locate this target using optimal moves. Once it is localized, we then remove the contribution of this target from the array data by using the CLEAN algorithm, and proceed to find the next strongest target, repeating these operations until all possible targets are localized. In order to determine that there are no targets remaining, a power distribution function is proposed based on the metric in [35]. It uses the array data at the probe phase only.

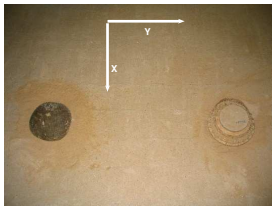

Fig. 15. Experiment M-2 setup with a VS-2.2 landmine and a rock of comparable size at the same distance from the source.

$$P(\mathbf{p}, \omega_l) = \sum_{l=1}^{N} \frac{|\mathbf{g}^H(\mathbf{p}, \omega_l)\mathbf{y}(\omega_l)|^2}{\|\mathbf{g}(\mathbf{p}, \omega_l)\|^2} \qquad (21)$$

This power distribution is calculated for positions $\mathbf{p}$ in the area of interest, using the Green's function vector (steering vector) $\mathbf{g}(\mathbf{p}, \omega_l)$ and $\mathbf{y}(\omega_l)$ is the array data at frequency ω_l.

For a stopping criterion, a scalar metric is calculated based on the matrix norm of $P(\mathbf{p}, \omega_l)$—the Euclidean norm (L_f). When there are strong targets present in a uniform background, we get a distribution with higher values for L_f. However, once we locate the targets, and remove their contributions from the array data, the power distribution decreases along with the values of the norm. Hence, one way to decide when to stop is to calculate this distribution along with the matrix norm, after localizing each target. If the values in the metric become very small compared to the starting value, then this indicates that no stronger targets remain.

To simulate this scenario, an AT mine (VS-2.2) and a rock of nearly same size and shape, Fig. 15, are buried at a depth of 6 cm. Both of these targets are at nearly the same distance from the source, with the rock being slightly closer. Assuming that there is only one target, we let the array maneuver optimally. After three iterations, the rock, which is stronger in this case is localized as shown in Fig. 16(a). After this, the same steps are repeated, with the contributions of the already localized target removed from the array. This time the array moves toward the second target (the AT mine) and localizes it in three optimal moves as shown in Fig. 16(b).

After each probe phase we calculate the power distribution and its norm. At first there are two strong targets. The histogram of this power distribution is shown in Fig. 17(a), with a calculated norm of 31.58. Once this target is localized, we remove its contribution from the array at the same probe position. The second power histogram is shown in Fig. 17(b) with a norm value of 12.45. The third power histogram when both targets have been removed is shown in Fig. 17(c), and the calculated norm value is 7.24. This final norm value should be the same as for an empty sandbox and can be used to define a stopping criterion (see Table I).

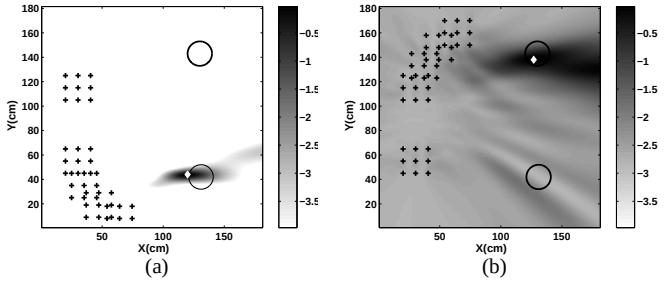

Fig. 16. Experiment M-2: VS-2.2 mine and a large rock. (a) The first target localized is the strongest target, in this case the rock. (b) After "CLEAN"-ing the data, the algorithm locates the second strongest target, which in this case is an AT mine. ML surfaces, the inverse of $\boldsymbol{J(z)}$, are plotted on a dB scale.

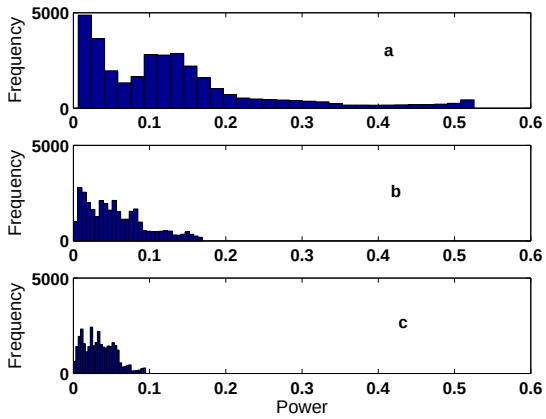

Fig. 17. Experiment M-2: Power histogram at the probe phase. (a) With both targets present. (b) With one strong target removed (the rock). (c) With both strong targets removed (both the mine and the rock).

E. Stopping Criterion for Multi-target Cases

Based on the two previous examples we can formulate a general strategy for dealing with multi-target cases when we don't have *a priori* knowledge about the number of targets. As we locate the targets one at a time and remove the strongest target with the CLEAN algorithm, we return to the probe stage and recalculate the power distribution, along with its norm. As we remove each localized target contribution from the array, the power values will decrease. This reduction can be used as a guide for stopping if we know the metric values for an empty sandbox. Using several different experiments, we summarize the power values in Table I. The metric converges to nearly the same value (approximately 7.5) after the processing removes all the strong targets. This lower limit value corresponds to an empty sandbox, when there are no targets present.

For the stopping criterion we will use a threshold that is within $\pm 10\%$ of the empty sandbox value ($L_f = 7.5$). For example, consider the data set with a single TS-50 AP mine, which is Case 4 in Table I. Its value with the contribution of the mine removed from the array is $L_f = 7.41$ which is within 10% of 7.5. In a realistic situation, the power distribution will depend upon various factors including the propagation properties of the medium, the dynamic range of the seismic source, as well as the target types, sizes and burial depths. Therefore, we would have to calibrate the array by using an area without any targets to calculate the benchmark metric values for the stopping criterion.

TABLE I

ESTIMATED NORM VALUES FOR POWER DISTRIBUTION FOR DIFFERENT MULTI-TARGET SCENARIOS.

	L_f
Case 1: Single AT mine and large rock (M-2)	
Initial	31.58
Rock removed	12.45
Rock and AT mine removed	7.24
Case 2: Single AP mine and 4 rocks	
Initial	19.39
Rock removed	11.6
AT mine and one rock removed	7.98
Case 3: Single AT mine and 9 rocks	
Initial	22.077
AT Mine removed	12.762
AT mine and big rock at 10 cm removed	8.19
Case 4: Single AP mine (Experiment S-1)	
Initial	13.07
AP Mine removed (empty sandbox)	7.41

F. Lateral Soil Inhomogeneity

Sometimes the soil properties will vary laterally due to changes in the soil composition and/or compaction. This can easily occur on a dirt or gravel road where the soil is packed more densely in the tracks by the vehicular traffic. The seismic wave velocity in the tracks is generally higher than in the surrounding regions. With such a velocity change, the waves will take a curved route instead of propagating on a straight path. This can direct the incident wave away from the mine or cause an error in the predicted mine location because the imaging algorithm assumes the waves travel in a straight path. An experiment was performed to investigate how the optimal maneuvering algorithm would handle such a case. A diagram of the experiment is shown in Fig. 18(a) where a TS-50 mine is buried at a depth of 1 cm, and the water content plus sand packing was selectively adjusted to form a high velocity region. This caused a significant portion of the wave to be directed away from the mine. The field intensity in the path was 12 dB stronger than that incident on the mine. Also the wave curves slightly away from the mine. The results of applying optimal maneuvering to this case are shown in Fig. 18(b). The algorithm still converges quickly to the location of the mine (in three optimal moves) even in the presence of the lateral inhomogeneity. Even though most of the energy in the surface wave is diverted away from the mine location, there is enough reflected energy for the algorithm to make its first move in the correct direction after which the location becomes easier.

IV. SUMMARY

The algorithm presented in this paper shows that it is feasible to control a maneuvering array to find buried targets like landmines. The experiments showed that the maneuvering system tends to find the strongest reflecting target, but it is able to find multiple targets and estimate the number of targets from the data. The algorithm starts from an initial estimate given by a probe phase, but as long as the probe phase gives some indication of energy from the approximate direction of the target, the array maneuvers will improve the location estimate.

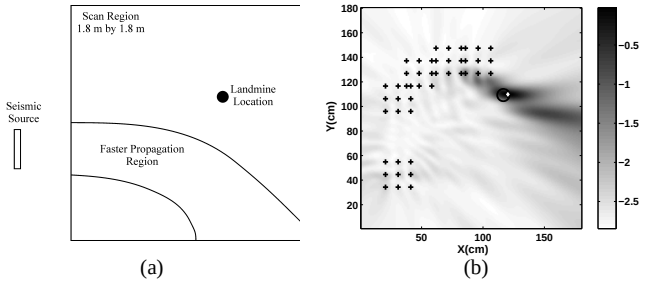

Fig. 18. Lateral inhomogeneity experiment. (a) Layout showing the mine location and the region of higher velocity. (b) Location results for a TS-50 mine buried at a depth of 1 cm after three optimal moves. The ML surface, the inverse of $\boldsymbol{J}(\mathbf{z})$, is plotted on a dB scale.

Although the optimal maneuver method developed here is for one source and one moving array, this strategy could be extended to multiple cooperating sources and receivers. The benefit would be faster coverage of larger regions if all the sources and receivers were mounted on individual robots. In order to exploit this configuration, it would be necessary to develop a distributed optimal maneuvering algorithm.

Future work must also address the identification problem to distinguish a landmine from a strong clutter reflector. After the target is located, the array would be positioned on top of a potential landmine to measure the induced resonance [7] and make the confirmation. The resonance feature could be enhanced with an imaging algorithm that generalizes the method in [10].

REFERENCES

[1] W. R. Scott, Jr., G. D. Larson, J. S. Martin, and G. S. M. II, "Field testing and development of a seismic landmine detection system," in *SPIE Proc*, vol. 5089, Orlando, FL, April 2003.

[2] W. R. Scott, Jr., J. S. Martin, and G. D. Larson, "Experimental model for a seismic landmine detection system," *IEEE Trans. Geoscience and Remote Sensing*, vol. 39, pp. 1155–1164, June 2001.

[3] J. Cook and J. J. Wormser, "Semi-remote acoustic, electric and thermal sensing of small buried nonmetallic objects," *IEEE Trans. Geosci. Remote Sensing*, vol. 11, pp. 135–152, 1973.

[4] "Feasibility of acoustic landmine detection: Final technical report," BBN, Tech. Rep. No. 7677, May 1992.

[5] P. Smith, P. S. Wilson, F. W. Bacon, J. F. Manning, J. A. Behrens, and T. G. Muir, "Measurement and localization of interface wave reflections from a buried target," *J. Acoust. Soc. Am.*, vol. 100, pp. 2333–2343, 1998.

[6] J. M. Sabatier and N. Xiang, "An investigation of acoustic-to-seismic coupling to detect buried antitank landmines," *IEEE Trans. Geosci. Remote Sensing*, vol. 39, pp. 1146–54, July 2001.

[7] C. T. Schroder, "On the interaction of elastic waves with buried landmines: An investigation using the finite-difference time-domain method," Ph.D. dissertation, Georgia Institute of Technology, 2001.

[8] W. R. Scott, Jr., J. O. Hamblen, G. D. Larson, J. S. Martin, and G. Larson, "Large vibrometer arrays for seismic landmine detection,," in *SPIE Proc*, vol. 6217, Orlando, FL, April 2006.

[9] A. Lal, S. Aranchuk, V. Doushkina, E. Hurtado, C. Hess, J. Kilpatrick, D. L'Esperance, N. Luo, V. Markov, J. Sabatier, and E. Scott, "Advanced LDV instruments for buried landmine detection,," in *SPIE Proc*, vol. 6217, Orlando, FL, April 2006.

[10] A. Behboodian, W. R. Scott, Jr., and J. H. McClellan, "Signal processing of elastic surface waves for localizing landmines," in 33rd *Asilomar Conf. Signals, Systems, and Computers*, Pacific Grove, CA, 1999.

[11] V. V. Fedorov, Ed., *Theory of Optimal Experiments*. SIAM, 1972.

[12] J. Helferty and D. Mudgett, "Optimal observer trajectories for bearings only tracking by minimizing the trace of the Cramér-Rao lower bound," in *Proc.* 32nd *IEEE Conf. Decision and Control*, San Antonio, TX, USA, Dec. 1993, pp. 936–939.

[13] J. Helferty, D. Mudgett, J. Dzielski, and J. Kauffmann, "Trajectory optimization for minimum range error in bearings-only source localization," in *Proc. Engineering in Harmony with Ocean*, vol. 2, Victoria ,BC, Canada, Oct. 1993, pp. 229–234.

[14] Y. Zhou, B. Porat, and A. Nehorai, "Localizing vapor-emitting sources by moving sensor," *IEEE Trans. Signal Processing*, vol. 44, no. 4, pp. 2655–2666, May 1996.

[15] X. Liao and L. Carin, "Application of the theory of optimal experiments to adaptive electromagnetic-induction sensing of buried targets," *IEEE Trans. Pattern Analysis and Machine Intelligence*, vol. 26, pp. 961–972, Aug. 2004.

[16] S. Begot, E. Voisin, E. Artioukhine, and J. Kauffmann, "D-optimal experimental design applied to linear magnetostatic inverse problem," *IEEE Trans. Magnetics*, vol. 38, no. 2, pp. 1065–1068, Mar. 2002.

[17] S. W. Lang, A. L. Kurkjian, J. H. McClellan, C. F. Morris, and T. W. Parks, "Estimating slowness dispersion from arrays of sonic logging waveforms," *Geophysics*, vol. 52, no. 4, pp. 530–544, April 1987.

[18] M. Alam, J. H. McClellan, and W. R. Scott, Jr., "Multi-channel spectrum analysis of surface waves," in *37th Asilomar Conf. Signals, Systems, and Computers*, Pacific Grove, CA, 2003.

[19] K. Steiglitz and L. E. McBride, "A technique for the identification of linear systems," *IEEE Trans. Automat. Contr.*, vol. 10, pp. 461–464, Oct. 1965.

[20] Y. Bresler and A. Macovski, "Exact maximum likelihood parameter estimation for superimposed exponential signals in noise," *IEEE Trans. Acoust., Speech, Signal Processing.*, vol. 34, pp. 1081–1089, Oct. 1986.

[21] J. H. McClellan and D.-W. Lee, "Exact equivalence of the Steiglitz-McBride iteration and IQML," *IEEE Trans. Signal Processing*, vol. 39, no. 2, pp. 509–512, 1991.

[22] M. Alam, J. H. McClellan, and W. R. Scott, Jr., "Spectrum analysis of seismic surface waves and its applications in seismic landmine detection," *submitted to J. Acoust. Soc. Am.*, Jan. 2006.

[23] M. Alam and J. H. McClellan, "Near field imaging of subsurface targets using active arrays and elastic waves," in *11th IEEE DSP Workshop*, vol. 5415, Taos Ski Valley, NM, Aug. 2004.

[24] M. Alam, J. H. McClellan, P. Norville, and W. R. Scott, Jr., "Time-reverse imaging for the detection of landmines," in *SPIE Proc*, vol. 5415, Orlando, FL, April 2004.

[25] M. Alam and J. H. McClellan, "Near field imaging of subsurface targets using wide-band multi-static RELAX/CLEAN algorithms," in *ICASSP 2005*, Philadelphia, Mar, 2004.

[26] C. Prada and J. Thomas, "Experimental subwavelength localization of scatterers by decomposition of the time reversal operator interpreted as a covariance matrix," *J. Acoust. Soc. Am.*, vol. 114, pp. 235–243, 2003.

[27] D. H. Johnson and D. E. Dudgeon, *Array Signal Processing: Concepts and Techniques*. Prentice Hall, 1993.

[28] L. Borcea, G. Papanicolaou, C. Tsokgka, and J. Berryman, "Imaging and time reversal in random media," *Inverse Problems*, vol. 18, pp. 1247–1279, 2002.

[29] V. Cevher, "A Bayesian framework for target tracking using acoustic and image measurements," Ph.D. dissertation, Georgia Institute of Technology, 2005.

[30] M. Westebbe, J. F. Bohme, H. Krummel, and M. B. Matthews, "Model fitting and testing in near surface seismics using maximum likelihood in frequency domain," in 32nd *Asilomar Conf. Signals, Systems, and Computers*, vol. 2, Pacific Grove, CA, 1999, pp. 1311–1315.

[31] R. Bachrach and A. Nur, "High-resolution shallow-seismic experiments in sand, Part I: Water table, fluid flow, and saturation," *Geophysics*, vol. 63, no. 2, pp. 1225–1233, Feb. 1998.

[32] R. Bachrach, J. Dvorkin, and A. Nur, "High-resolution shallow-seismic experiments in sand, Part II: Velocities in shallow unconsolidated sand," *Geophysics*, vol. 63, no. 2, pp. 1234–1240, Feb. 1998.

[33] J. M. Sabatier, H. E. Bass, L. N. Bolen, and K. Attenborough, "Acoustically induced seismic waves," *J. Acoust. Soc. Am.*, vol. 80, pp. 646–649, 1986.

[34] J. S. Martin, G. Larson, and W. R. Scott, Jr., "Seismic detection of buried landmines using surface-contacting sensors," *submitted to J. Acoust. Soc. Am.*, Jan. 2006.

[35] Y. Wang, J. Li, P. Stoica, M. Shepalk, and T. Nishida, "Wideband relax and wideband clean for aeroacoustic imaging," *J. Acoust. Soc. Am.*, vol. 115(2), pp. 757–767, 2004.